Author Manuscript Author Manuscript Author Manuscript Author Manuscript

HHS Public Access
Author manuscript
*ACS Appl Mater Interfaces*. Author manuscript; available in PMC 2022 January 04.

Published in final edited form as:
*ACS Appl Mater Interfaces*. 2019 May 22; 11(20): 18233–18241. doi:10.1021/acsami.9b04362.

# Reference-Free Traction Force Microscopy Platform Fabricated via Two-Photon Laser Scanning Lithography Enables Facile Measurement of Cell-Generated Forces

**Omar A. Banda**[†], **Chandran R. Sabanayagam**[‡], **John H. Slater**[*,†]

[†]Department of Biomedical Engineering, University of Delaware, 5 Innovation Way, Newark, Delaware 19711, United States

[‡]Delaware Biotechnology Institute, University of Delaware, 15 Innovation Way, Newark, Delaware 19711, United States

## Abstract

Cells sense and respond to the physical nature of their microenvironment by mechanically probing their surroundings via cytoskeletal contractions. The material response to these stresses can be measured via traction force microscopy (TFM). Traditional TFM platforms present several limitations including variable spatial resolution, difficulty in attaining the full three-dimensional (3D) deformation/stress profile, and the requirement to remove or relax the cells being measured to determine the zero-stress state. To overcome these limitations, we developed a two-photon, photochemical coupling approach to fabricate a new TFM platform that provides high-resolution control over the 3D placement of fluorescent fiducial markers for facile measurement of cell-generated shear and normal components of traction forces. The highly controlled placement of the 3D marker array provides a built-in, zero stress state eliminating the need to perturb the cells being measured while also providing increased throughput. Using this platform, we discovered that the magnitude of cell-generated shear and normal force components are linked both spatially and temporally. The facile nature and increased throughput of measuring cell-generated forces afforded by this new platform will be useful to the mechanotransduction community and others.

## Graphical Abstract

---

[*]**Corresponding Author,** jhslater@udel.edu.

Supporting Information
The Supporting Information is available free of charge on the ACS Publications website at DOI: 10.1021/acsami.9b04362.

Notes
The authors declare no competing financial interest.

Author Manuscript

Author Manuscript

Author Manuscript

Author Manuscript

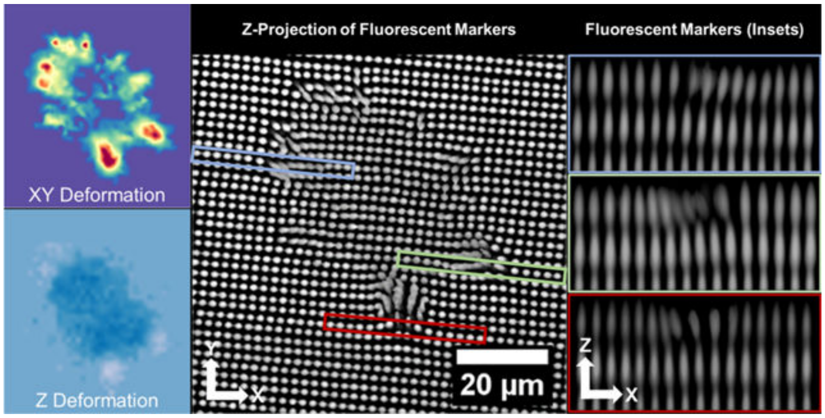

**Keywords**

hydrogel; cytoskeletal tension; multiphoton lithography; mechanotransduction; cell patterning

## INTRODUCTION

Traction force microscopy (TFM) has become the standard method to measure cell-generated forces and investigate the role these forces play in mediating cell behavior. TFM has been implemented to investigate the influences of cytoskeletal tension and/or traction forces in regulating cell proliferation,[1–3] differentiation,[4–9] migration,[10–12] nuclear polarization,[13] nuclear deformation,[14–16] and reaction to drugs.[17] Although cell-generated shear components of traction are usually measured, the magnitude of the out-of-plane, normal components can reach 50% of in-plane, shear components.[12,18] Normal components of traction play an important role in cellular processes including leukocyte extravasation[19] and may also influence cell fate via nuclear deformation and chromatin remodeling.[14,15,20,21] Accordingly, the ability to accurately and easily measure out-of-plane, normal components, along with shear components, is of great interest to many areas of research.

The most common platform capable of measuring out-of-plane, normal tractions utilizes protein- or peptide-functionalized elastomeric materials, usually polyacrylamide, containing embedded micro- or nanometer-sized fluorescent spheres that act as fiducial markers to measure material deformation.[18,22,23] These platforms are straightforward to fabricate and characterize and provide high-resolution traction measurements through the use of densely packed fluorescent spheres.[24] A limitation of this approach is the lack of control over fiducial marker placement and spacing. This lack of control can induce a number of spacing-related issues.[25] For example, markers may be too close together to be accurately resolved or too far apart as to create unusable regions, together inducing regionally biased resolution in material deformation measurements and subsequent force/stress calculations. Random marker placement also necessitates acquisition of a zero-stress state reference image to be registered with the deformation images for displacement measurements, requiring physical removal of the cells being examined or chemical perturbation to relax their cytoskeletal

Author Manuscript Author Manuscript Author Manuscript Author Manuscript

tension. This necessity hinders long-term cell studies and prevents subsequent cellular analyses.

To overcome some of these limitations, several reference-free platforms have been generated using micromolding and other high-resolution fabrication techniques.[17,26–29] The most commonly implemented method in this category utilizes micromolded pillar arrays to approximate cellular tractions based on the deflection of pillars in response to cell-generated tension. The reference position of the surface of the pillars is approximated based on the location of the pillar base. Pillar-based methods greatly facilitate measures of cell-induced shear components but are limited to two-dimensional (2D) measures. Reference-free platforms capable of measuring out-of-plane deformations implement patterned arrays of fluorescent fiducial markers on the surface of an elastomeric substrate with high spatial resolution and fidelity. The patterned marker surface array can serve as a built-in, implied, zero-stress reference state. The implied reference provides the ability to measure cell-induced material deformation using a single three-dimensional (3D) image acquisition, without physically removing or chemically perturbing the cells, thereby enabling facile use of standard cell analysis techniques, including immunofluorescence labeling, in combination with TFM.[26,30]

We developed an alternative reference-free platform using a photolithographically patterned hydrogel containing a built-in, implied reference state to measure the complete 3D material deformation profile induced by cells. The platform allows for continuous capture of material deformation without chemically relaxing or physically removing the cells. This facilitates temporal measurements of the same cell population over extended time as well as the ability to analyze a relatively large cell population providing higher throughput. The platform utilizes a 3D array of fluorescent fiducial markers embedded in a base hydrogel. Two-photon laser scanning lithography (TP-LSL)[31–36] is implemented to photocouple fluorescently labeled, poly(ethylene glycol) monoacrylate macromers into a base hydrogel composed of poly(ethylene glycol) diacrylate (PEGDA) (Figure 1). The resulting markers are ellipsoidal in shape with a 3D profile dictated by the point spread function of the pulsed laser. Reference positions for displaced markers are approximated using linear fits of surrounding nondisplaced markers resulting in a digital reconstruction of the zero-stress state. We demonstrate that using this implied reference state allows facile measurement of shear and normal components of cell-generated tractions using a single volumetric image stack. Using this platform, we quantified material deformation profiles and forces induced by individual human umbilical vein endothelial cells (HUVECs) as well as small HUVEC clusters. Consistent with a previous study, we observe that the extent of the shear component of traction generated by individual cells is positively correlated with increased spreading.[37] We further demonstrate that the normal component induced by individual cells follows a similar trend and that shear and normal components are tightly linked both in magnitude and temporally. Cell clusters display weaker correlations of shear and normal components of tractions with increased area, but the magnitude of shear and normal components are still tightly linked. We also demonstrate the ability to generate single-cell patterns via a second round of TP-LSL to photocouple PEG monoacrylates functionalized with integrin-binding peptide, arginine-glycine-aspartic acidserine (RGDS), to the hydrogel surface to control cell shape and spreading.

Author Manuscript Author Manuscript Author Manuscript Author Manuscript

## RESULTS

The platform consists of a base PEGDA hydrogel containing an embedded array of ellipsoidal fluorescent fiducial markers with Gaussian-like intensity profiles (Figure 2a–c). We chose PEGDA because of its protein-repulsive properties, biological inertness, and ease of chemical and mechanical manipulation. The size, shape, and intensity profile of the patterned fiducial markers are dictated by the numerical aperture of the objective as well as the intensity of the focused laser beam. Using a 740 nm, 140 fs pulse width, Ti:S laser operating at 80 MHz with a fluence of 3.7 nJ $\mu m^{-2}$ focused through a 1.2 numerical aperture water immersion objective resulted in ellipsoidal features with full-width, half maximum dimensions of 0.84 ± 0.11 $\mu m$ in $XY$ and 3.73 ± 0.30 $\mu m$ in $Z$. Marker spacing was prescribed in the $X$-direction by a digital mask (2.12 $\mu m$), in $Y$ by an automated image tiling step size (2.12 $\mu m$), and in $Z$ by an automated $Z$-stepping size for the objective turret motor (3.5 $\mu m$). The center-to-center marker spacing varied slightly from the dictated values as the spacing precision was dependent on the mode of stepping (image-guided galvometers vs stage motor vs objective turret motor). A spacing in $X$ of 2.19 ± 0.04 $\mu m$, $Y$ of 2.17 ± 0.14 $\mu m$, and $Z$ of 4.50 ± 0.30 $\mu m$ was typically achieved (Figure 2d), with a corresponding 2D fiducial marker density of 0.21 markers $\mu m^{-2}$ in $XY$ and 3D density of 0.05 markers $\mu m^{-3}$.

To determine the accuracy of using reference line fitting to establish marker centroid positions, the deviation of fiducial marker centroids in nonstressed hydrogels, without cells, was measured (Figure 2e,f; Figure S1), as well as in nondeformed regions sufficiently far enough away from cells as to not be displaced. The value representing two standard deviations from the mean displacement magnitude in each patterned region was used to characterize the accuracy and to set a lower limit threshold of displacement magnitude, which would reliably yield displacements of the correct orientation. Displacements falling below the threshold were treated as noise and suppressed. The threshold value was updated for each patterned region to account for possible variability. Typical accuracies were 127 ± 17 nm in the $XY$ plane and 140 ± 22 nm in $Z$.

To quantify stiffness of the hydrogels for traction force calculations, nanoindentation experiments were performed using a Bruker Bioscope Catalyst BioAFM (Figure 3). All curve fitting was performed using the Bruker NanoScope Analysis (see the Supporting Information). Of particular interest was whether addition of fluorescent fiducial markers had a measurable impact on hydrogel elasticity. The surface moduli for the patterned and nonpatterned hydrogels were 3.79 ± 0.12 and 4.05 ± 0.18 kPa, respectively. Although this difference was statistically significant, the functional impact of the difference was ignored because of its low magnitude. To account for the possibility that the observed differences were simply due to local variations in surface elasticity of the base hydrogel, a Young's modulus of 3.9 kPa representing an average of all measures and which is within 5% of all measured means was used for traction calculations.

To approximate the zero-stress state marker positions for a displacement data set, we interpolated reference positions for displaced markers from linear fits of nondisplaced markers within the same row or column (Figure 4b; see the Supporting Information). For any given marker, the intersection of linearfits of nondisplaced markers in the $X$-direction

Author Manuscript Author Manuscript Author Manuscript Author Manuscript

(rows) and in the $Z$-direction (columns) provided the 3D, nonstressed, reference coordinates needed to measure marker displacement. The reference lines running axially ($Z$-direction) through the hydrogel were used to measure the shear displacement in the $XY$ plane. A depth of 12 $\mu$m into the hydrogel, from the surface, was sufficient to reach nondisplaced markers with $XY$ coordinates that represented the zero-stress state location of displaced markers. To measure normal marker displacement, linear reference fits parallel to the hydrogel surface ($X$-direction) were used. A dilation of the cell boundary in $XY$ of 8.13 $\mu$m was sufficient to encompass, on average, >90% of all hydrogel deformation, so all markers beyond the boundary were designated nondisplaced for fitting reference lines. To convert marker displacements to surface tractions, we implemented a 3D TFM algorithm which utilizes a linear elastic material model with Young's modulus of 3.9 kPa and $\nu$ = 0.2 (Figure 4f–h).[38] A Poisson's ratio of 0.2 was chosen as it accurately describes small hydrogel surface deformations.[39–41] Prior to conversion, unfiltered deformation data were interpolated to a grid spacing equal to the sampling density of the fiducial marker arrays, which served as the input to the TFM code.

Using this new platform, many cells can be measured without concern for maintaining positional accuracy to collect a nonstressed, reference state image, thereby allowing for higher throughput. To demonstrate this, data were collected from more than 50 individual cells and 9 cell clusters over a 24 h period, including several time-lapse studies. As metrics to describe the total material deformation induced by a cell, surface displacements were interpolated to a grid spacing matching the sampling density of the original marker arrays. The sum of the displacement magnitudes in the $XY$ plane and in $Z$ are referred to as the sum of shear displacement and sum of normal displacement, respectively. To validate the platform, we reproduced a previously reported trend of linearly increased shear with increased cell spreading (Figure 5a).[37] As the platform allows facile measurement of normal components, we also examined this relationship and demonstrated that normal deformation and force follow similar linear trends with increased cell spreading (Figure 5b,h). To further investigate the relationship between shear and normal traction components, we examined their relative magnitude, spatial distribution, and temporal behavior. We found a positive correlation between shear and normal deformation and traction components for all cells measured, where the slope of a linear regression was 1.39 and 1.13 for the deformation and forces, respectively (Figure 5c). This prompted us to investigate how the normal and shear components were related spatially. The largest material deformation occurs at the cell periphery with shear components oriented toward the cell interior, upward normal components occurring distally, and downward normal components proximally (Figure 5d–f). The relative spatial organization of shear and normal components suggests a rotational moment occurring about the location of maximum shear, likely at focal adhesions, as has been previously reported.[12,18,42] The observed trends in displacement data held true for the converted traction data (Figure 5g–i). Time-lapse studies (Figure 6, Movies S1 and S2) demonstrate that the shear and normal traction components vary with time (Figure 6a,b) but that the relative ratio of shear to normal components stays nearly constant (Figure 6c), indicating that normal and shear components are linked in magnitude even temporally. We applied the same analysis to cell clusters (Figure 7). Interestingly, although small clusters did not always exhibit the same spatial distribution of shear and normal components as

Author Manuscript Author Manuscript Author Manuscript Author Manuscript

observed in individual cells (Figure S2), the overall ratio of shear to normal was consistent with that of individual cells with a linear regression slope of 1.39 and 1.08 for deformation and forces, respectively (Figure 7c). In addition, we observed the highest magnitude of the in-plane component of cellular tractions at the periphery of cell clusters, suggesting that cell–cell junctions propagate cell–matrix loads between cells in a cluster, consistent with previous studies.[43–45]

A common technique often coupled with TFM is micro-contact printing,[6,9,46,47] which provides control over adhesion ligand availability and subsequently cell spreading and shape. Using TP-LSL, the same control can be achieved at the hydrogel surface. The protein-repulsive nature of PEG provides a nonadhesive background for patterning cells. We implemented a second round of TP-LSL to photocouple an RGDS-functionalized PEG monoacrylate macromer to the surface of the TFM platform to generate arrays of single-cell patterns (Figure 8). We demonstrate the ability to culture adipose-derived stem cells on 50 $\mu$m diameter circular patterns and elongated, obround patterns which induced a high-tension state with strain concentrated at the rounded narrow ends.[6,46,47]

## DISCUSSION

We developed a reference-free platform containing a built-in, implied, zero-stress state that allows complete capture of cell-induced 3D material deformation and force profiles. The platform tracks material deformation as a function of centroid displacement of photolithographically patterned fluorescent fiducial markers embedded in a base hydrogel. The ability to capture both the reference state and displaced state in a single image stack greatly facilitates data collection allowing for a large cell population to be analyzed in a single experiment, thereby increasing throughput. It is important to note that circumventing the need for a reference image is not a new concept. A number of platforms exist that contain a built-in reference state achieved through implementing regular arrays of fiducial markers.[26,28,29,48–51] To achieve reference-free functionality, this platform uses a new approach to approximate the zero-stress state positions of fiducial markers. Developing the methodology to analyze displacements in this platform required characterizing the precision of the laser scanning microscope used for multiphoton chemical coupling. To minimize error, patterning dimensions that had the most consistent and predictable spacing of rows of markers were identified and linear fits of individual rows in these dimensions were used to determine reference locations of displaced markers (see the Supporting Information). Linear fits of columns through the $Z$-dimension accurately predict $X$ and $Y$ reference positions, and similarly, linear fits of rows through the $X$-dimension accurately predict $Y$ and $Z$ reference positions. The intersection of these two independent fits provides the 3D nonstressed, reference position for every marker in the data set.

As an example of this platform’s potential applications, we measured the 3D deformation profiles induced by HUVECs. Cells generate both in-plane and out-of-plane traction components, inducing 3D deformation in the underlying material. The spatial distribution, relative magnitude, and temporal linking suggest that both the in-plane and out-of-plane deformation are linked and may be a direct or indirect product of myosin-mediated cell contractility. On the basis of the distribution of normal material deformations beneath

Author Manuscript

Author Manuscript

Author Manuscript

Author Manuscript

adherent cells, we expect that normal deformation may be, at least in part, the result of the cellular cortex pressing into the hydrogel perhaps because of the mechanisms described previously in *Dictyostelium* cells.[12] However, we discovered that normal deformation was most commonly either near or coincident with large shear deformation, which may also suggest that some component of normal deformation is simply the material response of the hydrogel to a high-magnitude shear. This is reinforced by the cell cluster data, where the spatial distribution of measured deformation did not follow the same pattern as individual cells (Figure S2), although the linear relationship between shear and normal deformation and forces held. Although it is clear that cells are responsible for generating normal force, it is unclear how it may be translated into the cell and what role, if any, this force plays in determining cell behavior. However, recent studies have shown that adhesion sites under the nucleus are compressed[52] and that force applied to the nucleus results in nuclear deformation and chromatin remodeling which can impact cell fate.[14,15,20,21] We also presented material displacement data converted to tractions. Several strategies exist for this conversion that are applicable to the workflow presented here; the method we used was found to be most compatible with our existing code.[18,38] Regardless of the methodology used to convert these data, other studies suggest that describing cellular tension in terms of material displacement yield useful information on their own.[17,53]

Although the ubiquitous RGDS ligand was used in this study, essentially any desired peptide or protein which can be functionalized with a compatible acrylate-PEG linker can be coupled to or patterned on the surface in a similar manner. In this way, the platform affords control over cell area, shape, focal adhesion distribution, and other physical aspects which have demonstrated roles in mechanotransduction pathways. In addition, digital masks, rather than physical masters, are used to control pattern geometry allowing new and interesting patterns to be implemented quickly.[54–59]

Traction forces have recently been used to distinguish the response between diseased and normal airway smooth muscle cells to bronchoconstrictor drugs in a high-throughput manner, demonstrating the potential of cellular traction as a metric for drug screening applications.[17] Also, another reference-free approach recently demonstrated the ability to simultaneously measure cell-generated tractions and the phosphorylation state of paxillin by combining TFM with traditional immunofluorescence labeling.[26,30] Similar applications may be possible with the TFM platform described here which could potentially aid throughput of such investigations.

There are a couple of considerations to keep in mind when determining the proper marker spacing when using this platform which include the level of tension generated by the cells being measured and the hydrogel elasticity. The fluorescent markers are composed of the same material as the base hydrogel and therefore deform with the base hydrogel in response to cellular tractions. If spaced too close to each other, the markers may begin to overlap in cases of high substrate deformation, making accurate centroid detection difficult. This can be avoided by either increasing the marker spacing or increasing the hydrogel elasticity. Increasing marker spacing lowers resolution while increasing hydrogel elasticity leads to lower deformations. For the cell types used here, HUVECs and ASCs, cultured on a 4 kPa hydrogel, we determined that a 2.12 $\mu$m spacing in $X, Y$ provided enough spacing to avoid

Author Manuscript

Author Manuscript

Author Manuscript

Author Manuscript

marker overlap while providing sufficient resolution to describe the traction profiles. An approach to decrease marker spacing includes the incorporation of additional marker colors which has been implemented in bead-based and reference-free TFM platforms to increase resolution.[24,26]

With regard to fabrication time, although multiphoton lithography provides high-resolution, 3D control over photoinitiation events, it is a serial process limited by the speed in which photocoupling occurs. In this study, a write speed of 1.25 $\mathrm{mm}^2\ \mathrm{h}^{-1}$ was achieved and has since been improved to 1.9 $\mathrm{mm}^2\ \mathrm{h}^{-1}$ using a piezo-actuated z-axis stage controller. This current write speed allows fabrication of a 2.2 $\mathrm{mm}^2$ array of fiducial markers that extends 30 $\mu$m into the hydrogel, from the surface (nine layers of markers spaced at 3.5 $\mu$m) in 70 min.

## CONCLUSIONS

In summary, a new TFM platform was developed that offers complete control over 3D fiducial marker placement to simplify measurement of cell-induced normal and shear material deformation in individual cells, cell clusters, and patterned cells.

## Supplementary Material

Refer to Web version on PubMed Central for supplementary material.

## ACKNOWLEDGMENTS

O.A.B. was supported by funding from a NSF IGERT SBE2 fellowship (1144726), startup funds provided by the University of Delaware, and the National Institutes of Health/National Cancer Institute IMAT Program (R21CA214299). J.H.S. is supported by funding from the National Institutes of Health/National Cancer Institute IMAT Program (R21CA214299) and the National Science Foundation CAREER Award Program (1751797). Microscopy access was supported by grants from the NIH-NIGMS (P20 GM103446), the NSF (IIA-1301765), and the State of Delaware. The structured illumination microscope was acquired with funds from the State of Delaware Federal Research and Development Grant Program (16A00471). The LSM880 confocal microscope used for TP-LSL was acquired with a shared instrumentation grant (S10 OD016361).

## REFERENCES

(1). Rauskolb C; Sun S; Sun G; Pan Y; Irvine KD Cytoskeletal Tension Inhibits Hippo Signaling through an Ajuba-Warts Complex. Cell 2014, 158, 143–156. [PubMed: 24995985]

(2). Huang S; Chen CS; Ingber DE Control of Cyclin D1, P27Kip1, and Cell Cycle Progression in Human Capillary Endothelial Cells by Cell Shape and Cytoskeletal Tension. Mol. Biol. Cell 1998, 9, 3179–3193. [PubMed: 9802905]

(3). Provenzano PP; Keely PJ Mechanical Signaling through the Cytoskeleton Regulates Cell Proliferation by Coordinated Focal Adhesion and Rho GTPase Signaling. J. Cell Sci 2011, 124, 1195–1205. [PubMed: 21444750]

(4). Reilly GC; Engler AJ Intrinsic Extracellular Matrix Properties Regulate Stem Cell Differentiation. J. Biomech 2010, 43, 55–62. [PubMed: 19800626]

(5). Wen JH; Vincent LG; Fuhrmann A; Choi YS; Hribar KC; Taylor-Weiner H; Chen S; Engler AJ Interplay of Matrix Stiffness and Protein Tethering in Stem Cell Differentiation. Nat. Mater 2014, 13, 979–987. [PubMed: 25108614]

(6). Lee J; Abdeen AA; Tang X; Saif TA; Kilian KA Geometric Guidance of Integrin Mediated Traction Stress during Stem Cell Differentiation. Biomaterials 2015, 69, 174–183. [PubMed: 26285084]

Author Manuscript

Author Manuscript

Author Manuscript

Author Manuscript

(7). Steward AJ; Kelly DJ Mechanical Regulation of Mesenchymal Stem Cell Differentiation. J. Anat 2015, 227, 717–731. [PubMed: 25382217]

(8). Lv H; Li L; Sun M; Zhang Y; Chen L; Rong Y; Li Y. Mechanism of Regulation of Stem Cell Differentiation by Matrix Stiffness. Stem Cell Res. Ther 2015, 6, 103. [PubMed: 26012510]

(9). Tijore A; Cai P; N MH; Zhuyun L; Yu W; Tay CY; L CT; Chen X; Tan LP Role of Cytoskeletal Tension in the Induction of Cardiomyogenic Differentiation in Micropatterned Human Mesenchymal Stem Cell. Adv. Healthcare Mater 2015, 4, 1399–1407.

(10). Lombardi ML; Knecht DA; Dembo M; Lee J. Traction Force Microscopy in Dictyostelium Reveals Distinct Roles for Myosin II Motor and Actin-Crosslinking Activity in Polarized Cell Movement. J. Cell Sci 2007, 120, 1624–1634. [PubMed: 17452624]

(11). Plotnikov SV; Pasapera AM; Sabass B; Waterman CM Force Fluctuations within Focal Adhesions Mediate ECM-Rigidity Sensing to Guide Directed Cell Migration. Cell 2012, 151, 1513–1527. [PubMed: 23260139]

(12). Álvarez-González B; Meili R; Bastounis E; Firtel RA; Lasheras JC; del Álamo JC Three-Dimensional Balance of Cortical Tension and Axial Contractility Enables Fast Amoeboid Migration. Biophys. J 2015, 108, 821–832. [PubMed: 25692587]

(13). Kim K; Kim K; Ryu JH; Lee H. Chitosan-catechol: A polymer with long-lasting mucoadhesive properties. Biomaterials 2015, 52, 161–170. [PubMed: 25818422]

(14). Versaevel M; Grevesse T; Gabriele S. Spatial Coordination between Cell and Nuclear Shape within Micropatterned Endothelial Cells. Nat. Commun 2012, 3, 671. [PubMed: 22334074]

(15). Buxboim A; Irianto J; Swift J; Athirasala A; Shin J-W; Rehfeldt F; Discher DE Coordinated Increase of Nuclear Tension and Lamin-A with Matrix Stiffness Outcompetes Lamin-B Receptor That Favors Soft Tissue Phenotypes. Mol. Biol. Cell 2017, 28, 3333–3348. [PubMed: 28931598]

(16). Li Q; Makhija E; Hameed FM; Shivashankar GV Micropillar Displacements by Cell Traction Forces Are Mechanically Correlated with Nuclear Dynamics. Biochem. Biophys. Res. Commun 2015, 461, 372–377. [PubMed: 25911321]

(17). Pushkarsky I; Tseng P; Black D; France B; Warfe L; Koziol-White CJ; Jester WF; Trinh RK; Lin J; Scumpia PO; Morrison SL; Panettieri RA; Damoiseaux R; Di Carlo D. Elastomeric Sensor Surfaces for High-Throughput Single-Cell Force Cytometry. Nat. Biomed. Eng 2018, 2, 124–137. [PubMed: 31015629]

(18). Legant WR; Choi CK; Miller JS; Shao L; Gao L; Betzig E; Chen CS Multidimensional Traction Force Microscopy Reveals Out-of-Plane Rotational Moments about Focal Adhesions. Proc. Natl. Acad. Sci. U.S.A 2013, 110, 881–886. [PubMed: 23277584]

(19). Yeh Y-T; Serrano R; François J; Chiu J-J; Li Y-SJ; del Álamo JC; Chien S; Lasheras JC Three-Dimensional Forces Exerted by Leukocytes and Vascular Endothelial Cells Dynamically Facilitate Diapedesis. Proc. Natl. Acad. Sci. U.S.A 2018, 115, 133–138. [PubMed: 29255056]

(20). Cho S; Irianto J; Discher DE Mechanosensing by the Nucleus: From Pathways to Scaling Relationships. J. Cell Biol 2017, 216, 305–315. [PubMed: 28043971]

(21). Wang Y; Nagarajan M; Uhler C; Shivashankar GV Orientation and repositioning of chromosomes correlate with cell geometry-dependent gene expression. Mol. Biol. Cell 2017, 28, 1997–2009. [PubMed: 28615317]

(22). Sabass B; Gardel ML; Waterman CM; Schwarz US High Resolution Traction Force Microscopy Based on Experimental and Computational Advances. Biophys. J 2008, 94, 207–220. [PubMed: 17827246]

(23). Munevar S; Wang Y. -l.; Dembo M. Traction Force Microscopy of Migrating Normal and H-Ras Transformed 3T3 Fibroblasts. Biophys. J 2001, 80, 1744–1757. [PubMed: 11259288]

(24). Colin-York H; Shrestha D; Felce JH; Waithe D; Moeendarbary E; Davis SJ; Eggeling C; Fritzsche M. Super-Resolved Traction Force Microscopy (STFM). Nano Lett. 2016, 16, 2633–2638. [PubMed: 26923775]

(25). Colin-York H; Fritzsche M. The Future of Traction Force Microscopy. Curr. Opin. Biomed. Eng 2018, 5, 1–5.

(26). Bergert M; Lendenmann T; Zündel M; Ehret AE; Panozzo D; Richner P; Kim DK; Kress SJP; Norris DJ; Sorkine-Hornung O; Mazza E; Poulikakos D; Ferrari A. Confocal Reference Free Traction Force Microscopy. Nat. Commun 2016, 7, 12814.

Author Manuscript

Author Manuscript

Author Manuscript

Author Manuscript

(27). Schwarz US; Balaban NQ; Riveline D; Addadi L; Bershadsky A; Safran SA; Geiger B. Measurement of Cellular Forces at Focal Adhesions Using Elastic Micro-Patterned Substrates. Mater. Sci. Eng., C 2003, 23, 387–394.

(28). Tan JL; Tien J; Pirone DM; Gray DS; Bhadriraju K; Chen CS Cells Lying on a Bed of Microneedles: An Approach to Isolate Mechanical Force. Proc. Natl. Acad. Sci. U.S.A 2003, 100, 1484–1489. [PubMed: 12552122]

(29). Desai RA; Yang MT; Sniadecki NJ; Legant WR; Chen CS Microfabricated Post-Array-Detectors (MPADs): An Approach to Isolate Mechanical Forces. J. Visualized Exp 2007, 7, 311.

(30). Panagiotakopoulou M; Lendenmann T; Pramotton FM; Giampietro C; Stefopoulos G; Poulikakos D; Ferrari A. Cell Cycle-Dependent Force Transmission in Cancer Cells. Mol. Biol. Cell 2018, 29, 2528–2539. [PubMed: 30113874]

(31). Culver JC; Hoffmann JC; Poché RA; Slater JH; West JL; Dickinson ME Three-Dimensional Biomimetic Patterning in Hydrogels to Guide Cellular Organization. Adv. Mater 2012, 24, 2344–2348. [PubMed: 22467256]

(32). Hahn MS; Miller JS; West JL Three-Dimensional Biochemical and Biomechanical Patterning of Hydrogels for Guiding Cell Behavior. Adv. Mater 2006, 18, 2679–2684.

(33). Wylie RG; Ahsan S; Aizawa Y; Maxwell KL; Morshead CM; Shoichet MS Spatially Controlled Simultaneous Patterning of Multiple Growth Factors in Three-Dimensional Hydrogels. Nat. Mater 2011, 10, 799–806. [PubMed: 21874004]

(34). Wylie RG; Shoichet MS Three-Dimensional Spatial Patterning of Proteins in Hydrogels. Biomacromolecules 2011, 12, 3789–3796. [PubMed: 21853977]

(35). Wosnick JH; Shoichet MS Three-Dimensional Chemical Patterning of Transparent Hydrogels. Chem. Mater 2008, 20, 55–60.

(36). Luo Y; Shoichet MS A Photolabile Hydrogel for Guided Three-Dimensional Cell Growth and Migration. Nat. Mater 2004, 3, 249–253. [PubMed: 15034559]

(37). Reinhart-King CA; Dembo M; Hammer DA Endothelial Cell Traction Forces on RGD-Derivatized Polyacrylamide Substrata. Langmuir 2003, 19, 1573–1579.

(38). Toyjanova J; Bar-Kochba E; López-Fagundo C; Reichner J; Hoffman-Kim D; Franck C. High Resolution, Large Deformation 3D Traction Force Microscopy. PLoS One 2014, 9, No. e90976.

(39). Kalcioglu ZI; Mahmoodian R; Hu Y; Suo Z; Van Vliet KJ From Macro- to Microscale Poroelastic Characterization of Polymeric Hydrogels via Indentation. Soft Matter 2012, 8, 3393.

(40). Wang M; Hill RJ Electric-Field-Induced Displacement of Charged Spherical Colloids in Compressible Hydrogels. Soft Matter 2008, 4, 1048. [PubMed: 32907138]

(41). Kloxin AM; Kloxin CJ; Bowman CN; Anseth KS Mechanical Properties of Cellularly Responsive Hydrogels and Their Experimental Determination. Adv. Mater 2010, 22, 3484–3494. [PubMed: 20473984]

(42). Franck C; Maskarinec SA; Tirrell DA; Ravichandran G. Three-Dimensional Traction Force Microscopy: A New Tool for Quantifying Cell-Matrix Interactions. PLoS One 2011, 6, No. e17833.

(43). Maruthamuthu V; Sabass B; Schwarz US; Gardel ML Cell-ECM Traction Force Modulates Endogenous Tension at Cell-Cell Contacts. Proc. Natl. Acad. Sci. U.S.A 2011, 108, 4708–4713. [PubMed: 21383129]

(44). Ng MR; Besser A; Brugge JS; Danuser G. Mapping the Dynamics of Force Transduction at Cell–cell Junctions of Epithelial Clusters. eLife 2014, 3, No. e03282.

(45). Mertz AF; Che Y; Banerjee S; Goldstein JM; Rosowski KA; Revilla SF; Niessen CM; Marchetti MC; Dufresne ER; Horsley V. Cadherin-Based Intercellular Adhesions Organize Epithelial Cell-Matrix Traction Forces. Proc. Natl. Acad. Sci. U.S.A 2013, 110, 842–847. [PubMed: 23277553]

(46). Oakes PW; Banerjee S; Marchetti MC; Gardel ML Geometry Regulates Traction Stresses in Adherent Cells. Biophys. J 2014, 107, 825–833. [PubMed: 25140417]

(47). Rape AD; Guo W. -h.; Wang Y.-l. The Regulation of Traction Force in Relation to Cell Shape and Focal Adhesions. Biomaterials 2011, 32, 2043–2051. [PubMed: 21163521]

(48). Tong MH; Huang N; Zhang W; Zhou ZL; Ngan AHW; Du Y; Chan BP Multiphoton Photochemical Crosslinking-Based Fabrication of Protein Micropatterns with Controllable Mechanical Properties for Single Cell Traction Force Measurements. Sci. Rep 2016, 6, 20063.

Author Manuscript

Author Manuscript

Author Manuscript

Author Manuscript

(49). Spivey EC; Ritschdorff ET; Connell JL; McLennon CA; Schmidt CE; Shear JB Multiphoton Lithography of Unconstrained Three-Dimensional Protein Microstructures. Adv. Funct. Mater 2013, 23, 333–339.

(50). Fu J; Wang Y-K; Yang MT; Desai RA; Yu X; Liu Z; Chen CS Mechanical Regulation of Cell Function with Geometrically Modulated Elastomeric Substrates. Nat. Methods 2010, 7, 733–736. [PubMed: 20676108]

(51). Shiu J-Y; Aires L; Lin Z; Vogel V. Nanopillar Force Measurements Reveal Actin-Cap-Mediated YAP Mechanotransduction. Nat. Cell Biol 2018, 20, 262–271. [PubMed: 29403039]

(52). Rothenberg KE; Neibart SS; LaCroix AS; Hoffman BD Controlling Cell Geometry Affects the Spatial Distribution of Load Across Vinculin. Cell. Mol. Bioeng 2015, 8, 364–382.

(53). Stout DA; Bar-Kochba E; Estrada JB; Toyjanova J; Kesari H; Reichner JS; Franck C. Mean deformation metrics for quantifying 3D cell-matrix interactions without requiring information about matrix material properties. Proc. Natl. Acad. Sci. U.S.A 2016, 113, 2898–2903. [PubMed: 26929377]

(54). Slater JH; Miller JS; Yu SS; West JL Fabrication of Multifaceted Micropatterned Surfaces with Laser Scanning Lithography. Adv. Funct. Mater 2011, 21, 2876–2888. [PubMed: 29861708]

(55). Slater JH; Culver JC; Long BL; Hu CW; Hu J; Birk TF; Qutub AA; Dickinson ME; West JL Recapitulation and Modulation of the Cellular Architecture of a User-Chosen Cell of Interest Using Cell-Derived, Biomimetic Patterning. ACS Nano 2015, 9, 6128–6138. [PubMed: 25988713]

(56). Slater JH; West JL Fabrication of Multifaceted, Micropatterned Surfaces and Image-Guided Patterning Using Laser Scanning Lithography, 1st ed.; Elsevier Inc., 2014; Vol. 119.

(57). Heintz KA; Mayerich D; Slater JH Image-Guided, LaserBased Fabrication of Vascular-Derived Microfluidic Networks. J. Visualized Exp 2017, 119, 1–10.

(58). Heintz KA; Bregenzer ME; Mantle JL; Lee KH; West JL; Slater JH Fabrication of 3D Biomimetic Microfluidic Networks in Hydrogels. Adv. Healthcare Mater 2016, 5, 2153–2160.

(59). Shukla A; Slater JH; Culver JC; Dickinson ME; West JL Biomimetic Surface Patterning Promotes Mesenchymal Stem Cell Differentiation. ACS Appl. Mater. Interfaces 2016, 8, 21883–21892. [PubMed: 26674708]

Author Manuscript Author Manuscript Author Manuscript Author Manuscript

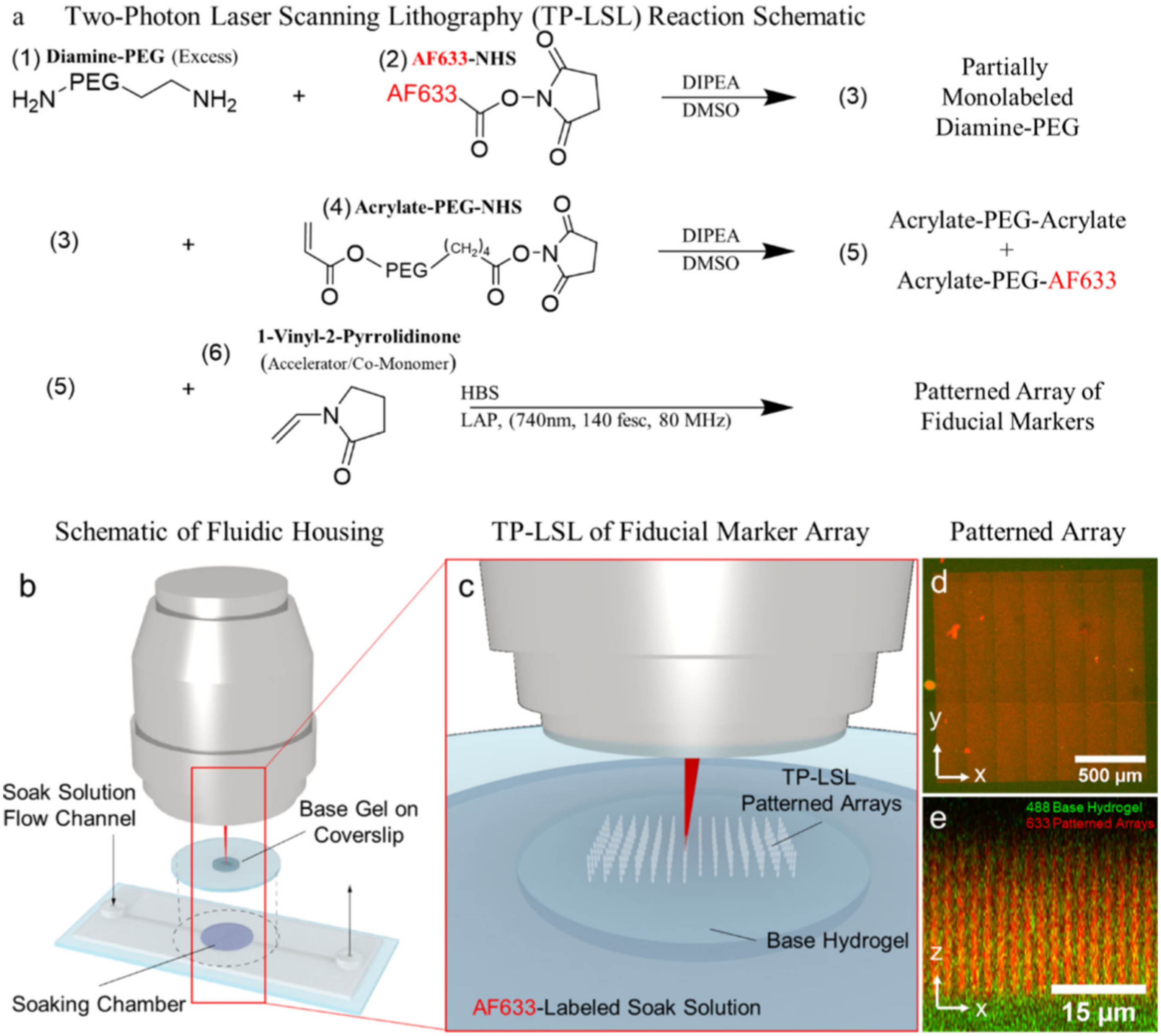

**Figure 1.**

Fabrication of the reference-free TFM platform. (a) Fluorophore-labeled PEG used to fabricate fiducial markers is synthesized by coupling a diamine-PEG to either an acrylate and a fluorophore or two acrylates using NHS esters. (b,c) Resulting acrylated-PEG species are photocoupled into a preformed hydrogel by soaking the hydrogel in a solution containing the PEG species, a radical generating photoinitiator (LAP), and a comonomer (NVP). (d,e) Resulting fiducial markers are patterned in large arrays within the upper ~20 $\mu$m of the base hydrogel.

Author Manuscript Author Manuscript Author Manuscript Author Manuscript

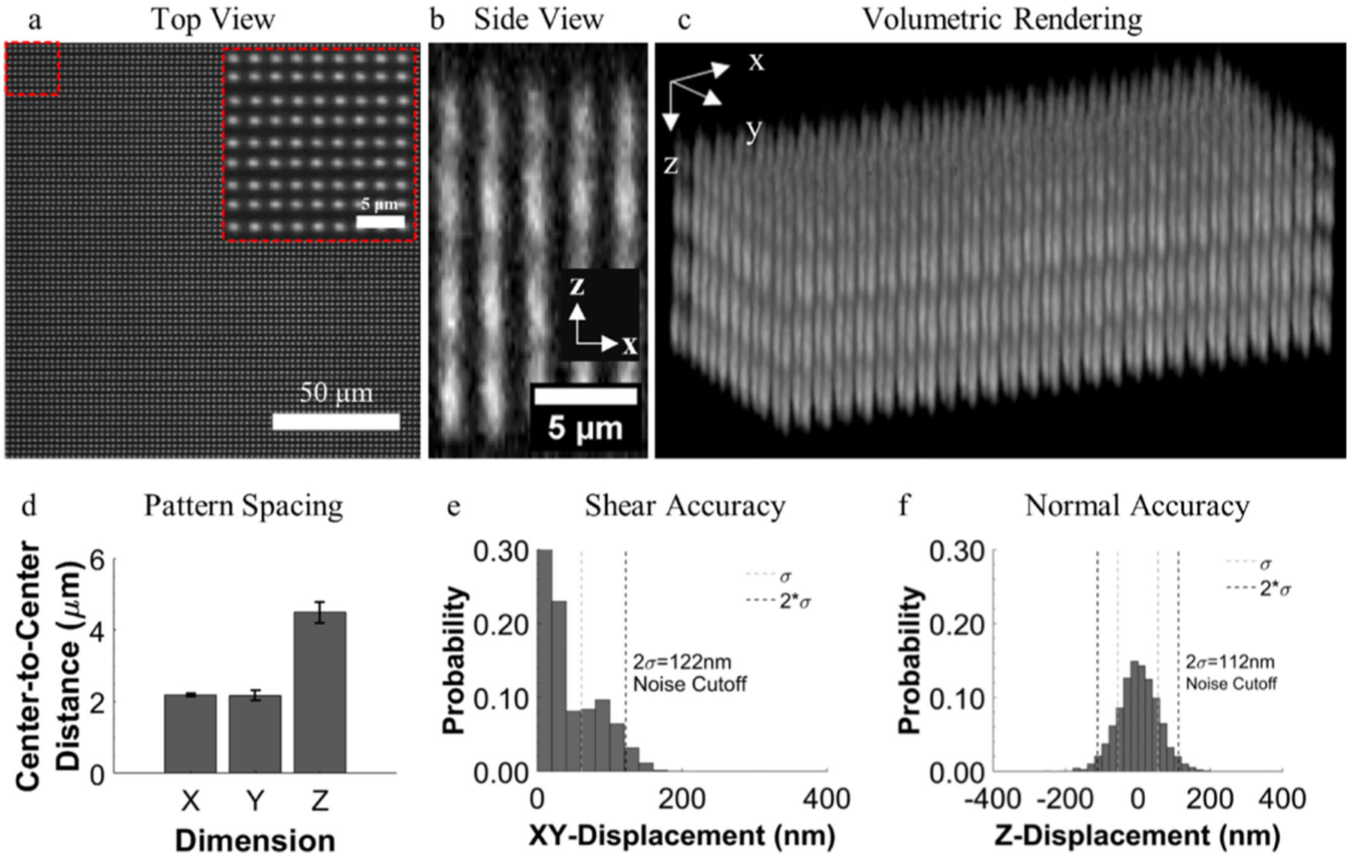

**Figure 2.**

Characteristics of the fiducial marker array. (a) Single view field of a patterned region with an inset demonstrating the consistency of the patterns. (b) Profile view and (c) volumetric rendering of a patterned region demonstrating the intensity profile of fiducial markers through the *Z*-direction that allows for centroid localization based on intensity fluctuations. (d) Mean spacing between fiducial markers in the patterned array. (e,f) Histograms demonstrating the accuracy of reference lines as a true reference, displayed as the probability of measuring fiducial marker displacement in a nondeformed marker array.

Author Manuscript Author Manuscript Author Manuscript Author Manuscript

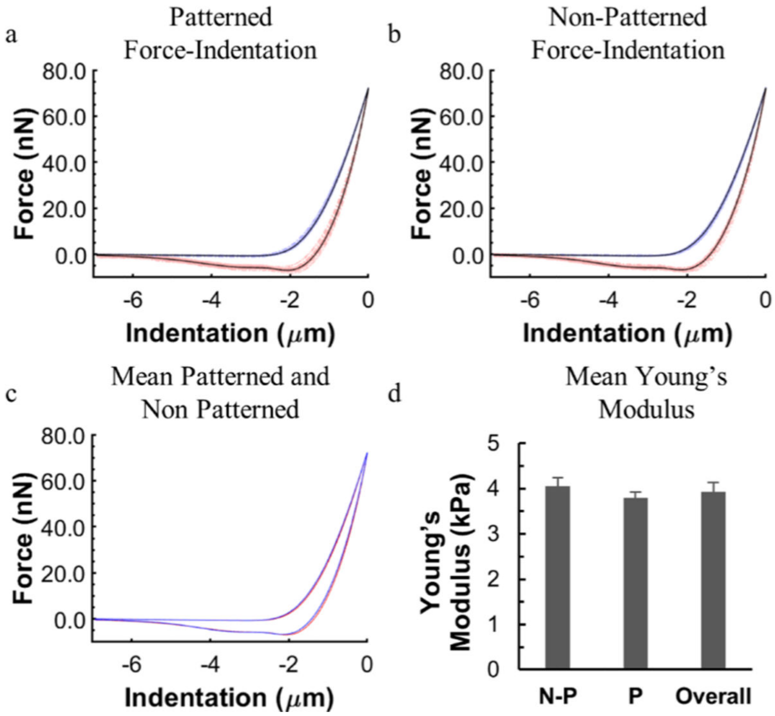

**Figure 3.**

Nanoindentation of PEGDA hydrogels to measure surface elasticity. Force indentation curves of (a) patterned and (b) nonpatterned hydrogels. Blue lines indicate approach, red lines indicate retraction, and black lines represent the average profile. (c) Overlay of the average indentation curves shows minimal difference between patterned and nonpatterned hydrogels. (d) Average Young's modulus determined from a Hertzian contact model for nonpatterned (N-P), patterned (P), and all regions (overall). *n* = 129 (66 patterned, and 63 nonpatterned).

Author Manuscript

Author Manuscript

Author Manuscript

Author Manuscript

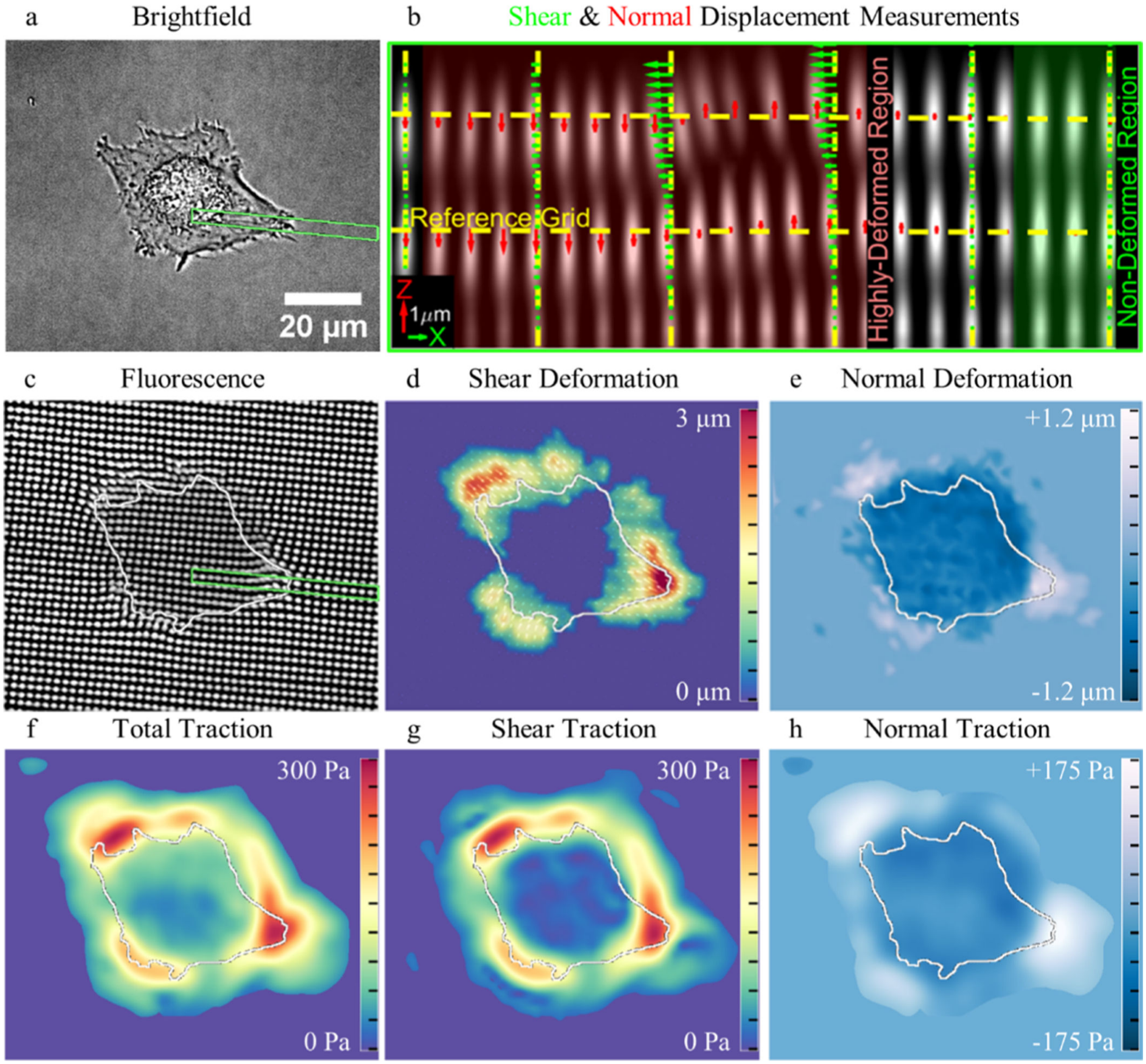

**Figure 4.**

Measuring 3D cell-induced hydrogel deformation and tractions. (a) Brightfield image of a HUVEC seeded on the surface of a patterned gel. (b) *XZ* profile view of the inset [green box in (a)] demonstrates how reference lines are used to measure shear and normal fiducial marker displacement. (c) *Z*-projection of the fluorescent markers below the adherent HUVEC demonstrates a clear representation of the measured displacements. Heatmaps of (d) shear and (e) normal deformation. Surface tractions are displayed as (f) total magnitude, (g) magnitude of shear component of tractions, and (h) normal component of tractions.

Author Manuscript
Author Manuscript
Author Manuscript
Author Manuscript

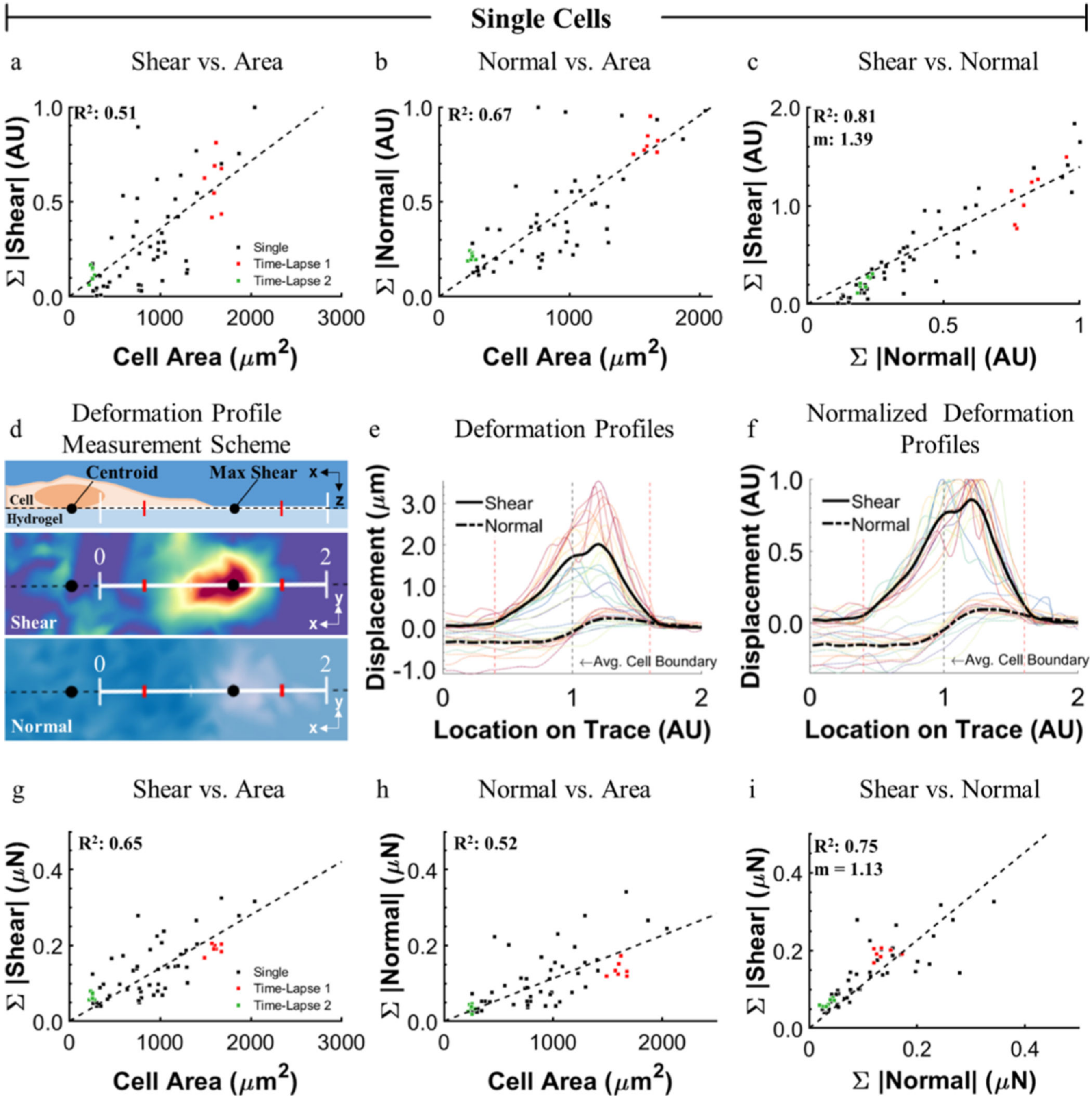

**Figure 5.**

Magnitudes and distributions of cell-induced hydrogel deformations and forces. Positive linear correlations exist between both (a) shear and (b) normal deformation with increased cell spreading for individual single cells. Black markers represent different individual cells and red and green markers are time-lapse measures of specific cells. (c) Strong linear correlation was observed between the sum of shear and normal deformation magnitudes (normalized to highest normal magnitude). *n* = 60 data points for (a–c). The distribution of shear and normal deformation was measured along a trace from the cell center through

Author Manuscript Author Manuscript Author Manuscript Author Manuscript

the maximum shear. (d) Lengths of the profiles were normalized so that the proximal and distal locations where the magnitude of shear was 20% of the maximum occurred at 0.4 and 1.6 (red ticks). (e,f) 22 profiles of shear and normal deformation, with the average plotted in black. The transition from negative to positive normal deformation occurs at the cell boundary, with maximum shear coinciding with maximum positive normal deformation. (g–i) Calculated shear and normal traction components corresponding to (a–c), respectively.

Author Manuscript

Author Manuscript

Author Manuscript

Author Manuscript

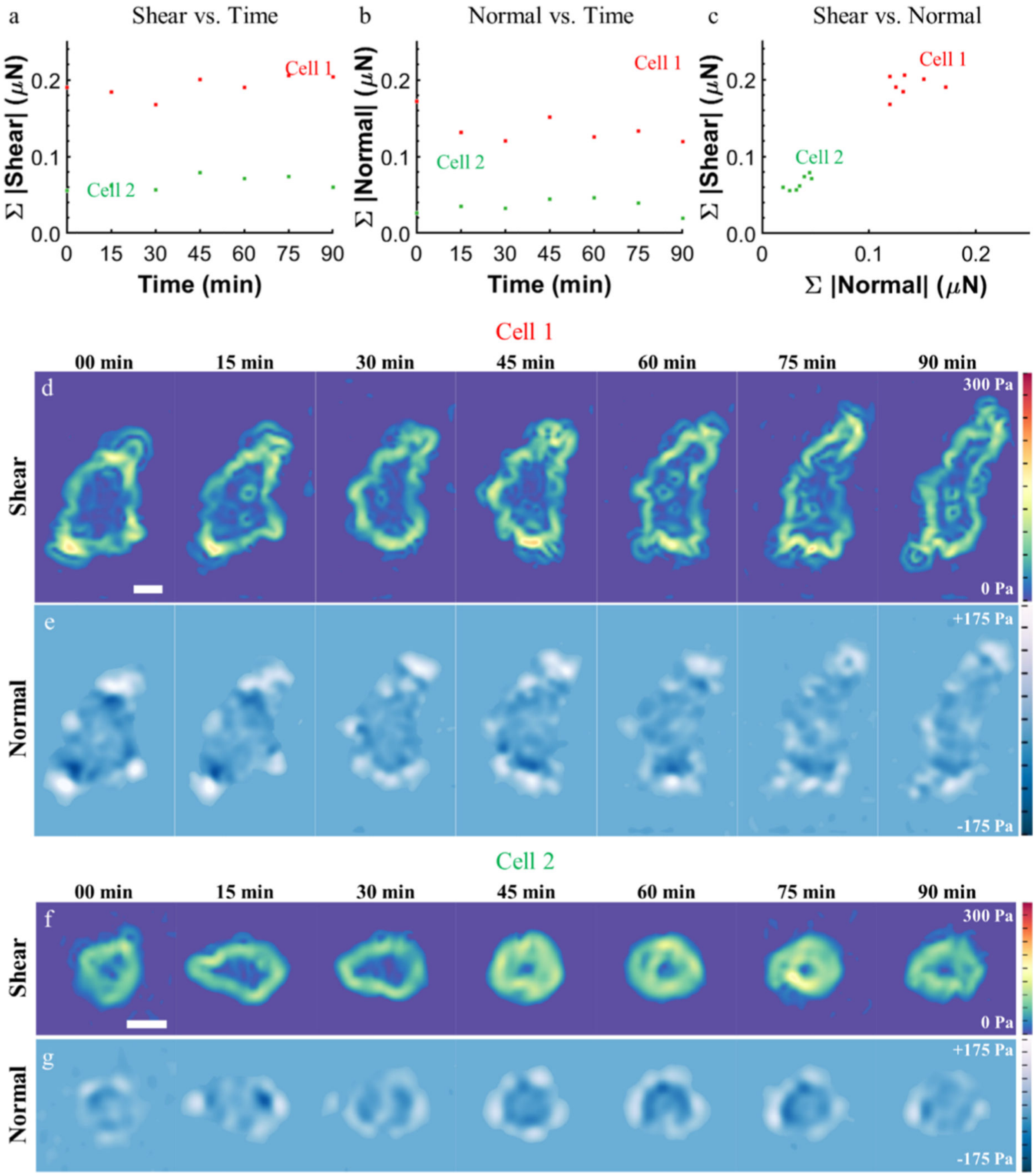

**Figure 6.**

Time-lapse, cell-induced hydrogel traction measurements. The sum of (a) shear and (b) normal components of traction for a well-spread cell (cell 1) and a spreading cell (cell 2) over 90 min at 15 min intervals. (c) Although shear and normal traction magnitudes vary with time, their magnitudes are linearly correlated at all time points. Heatmaps of (d,f) shear stress and (e,g) normal stress for cell 1 and cell 2. SB = 20 $\mu$m. See Movies S1 and S2.

Author Manuscript Author Manuscript Author Manuscript Author Manuscript

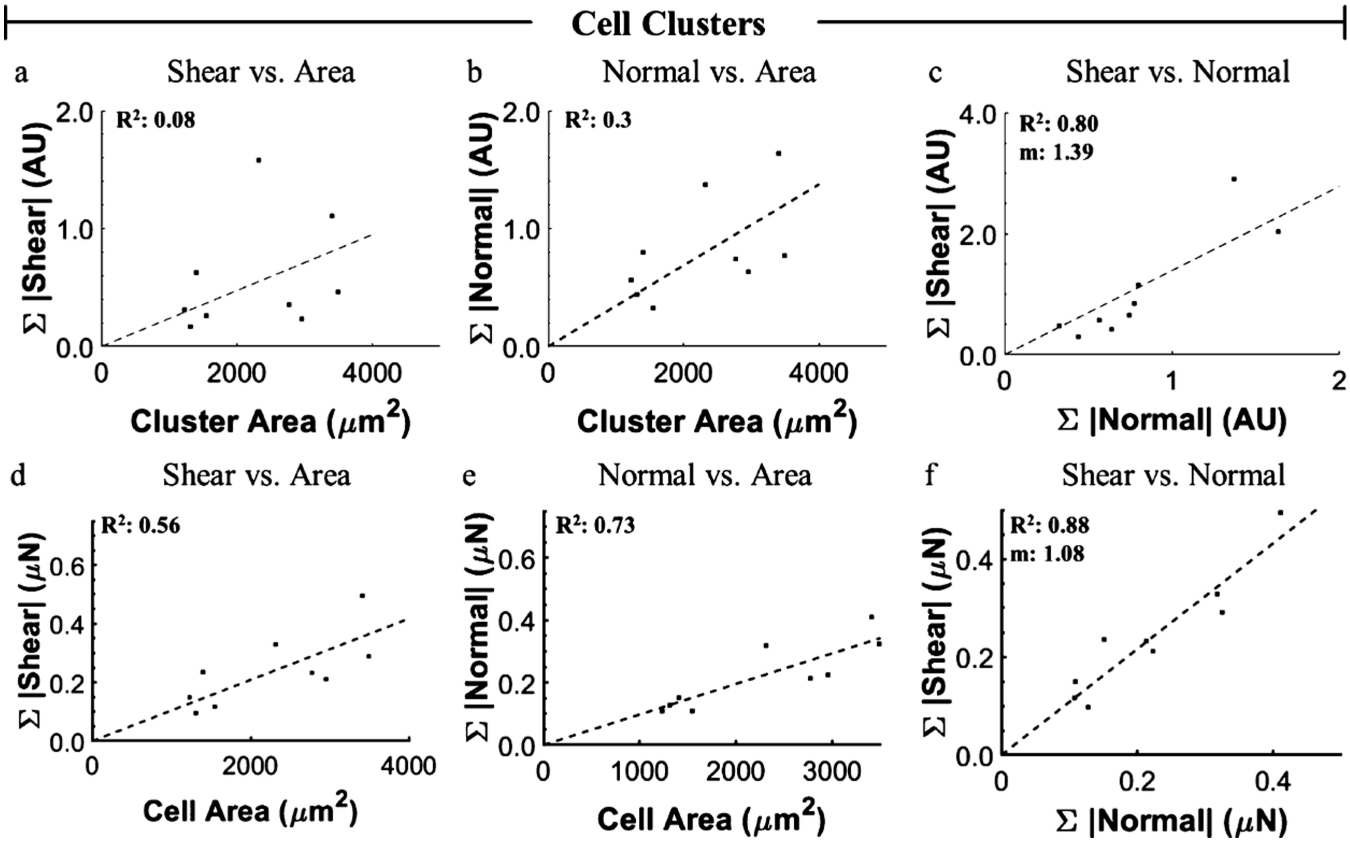

**Figure 7.**

Magnitudes and distributions of cell cluster-induced hydrogel deformations and forces. Cell clusters (*n* = 9) displayed similar trends between (a) shear and (b) normal deformation with spread area, as well as (c) shear vs normal, that was observed for individual cells. (a,b) are normalized to the highest value measured in the individual, single-cell data in the respective category (i.e., shear or normal). Shear and normal data in (c) are normalized to the highest normal deformation measured in individual cells. (d–f) Calculated forces corresponding to (a–c), respectively.

Author Manuscript

Author Manuscript

Author Manuscript

Author Manuscript

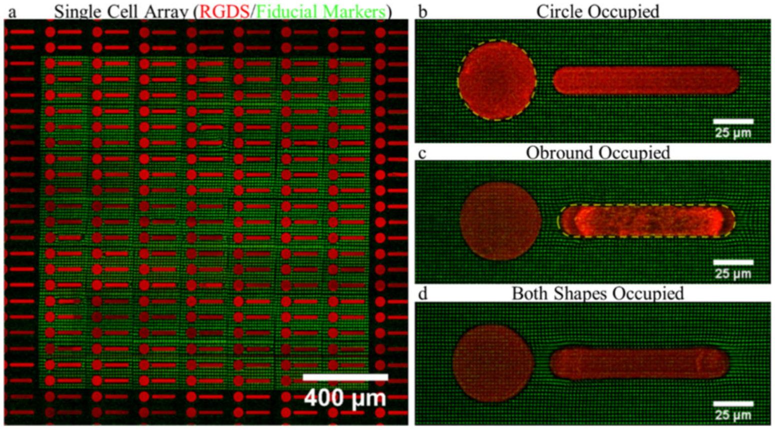

**Figure 8.**

Fabrication of single-cell pattern arrays. (a) Fluorescent image of an array of circle and obround patterns composed of an (red) acrylated RGDS peptide on top of (green) TFM fiducial markers. (b–d) *Z*-projections of several permutations of ASCs adhered to patterns demonstrate that a variety of deformation profiles can be imposed on the cells using two-photon lithography to augment TFM studies.